Acta Materialia 214 (2021) 117003

Contents lists available at ScienceDirect

Acta Materialia

journal homepage: www.elsevier.com/locate/actamat

Full length article

Unravelling the ion-energy-dependent structure evolution and its implications for the elastic properties of (V,Al)N thin films

Soheil Karimi Aghda[a,*], Denis Music[b], Yeliz Unutulmazsoy[c], Heng Han Sua[a], Stanislav Mráz[a], Marcus Hans[a], Daniel Primetzhofer[d], André Anders[c,e], Jochen M. Schneider[a]

[a] Materials Chemistry, RWTH Aachen University, Kopernikusstr. 10, 52074 Aachen, Germany
[b] Department of Materials Science and Applied Mathematics, Malmö University, 20506 Malmö, Sweden
[c] Leibniz Institute of Surface Engineering (IOM), Permoserstr. 15, 04318 Leipzig, Germany
[d] Department of Physics and Astronomy, Uppsala University, Lägerhyddsvägen 1, 75120 Uppsala, Sweden
[e] Felix Bloch Institute, Leipzig University, Linnéstr. 5, 04103 Leipzig, Germany

ARTICLE INFO

Article history:
Received 8 March 2021
Revised 4 May 2021
Accepted 13 May 2021
Available online 22 May 2021

Keywords:
Ion kinetic energy
Stress state
Point defects
Elastic modulus

ABSTRACT

Ion irradiation-induced changes in the structure and mechanical properties of metastable cubic (V,Al)N deposited by reactive high power pulsed magnetron sputtering are systematically investigated by correlating experiments and theory in the ion kinetic energy (E_k) range from 4 to 154 eV. Increasing E_k results in film densification and the evolution from a columnar (111) oriented structure at $E_k \leq 24$ eV to a fine-grained structure with (100) preferred orientation for $E_k \geq 104$ eV. Furthermore, the compressive intrinsic stress increases by 336 % to -4.8 GPa as E_k is increased from 4 to 104 eV. Higher ion kinetic energy causes stress relaxation to -2.7 GPa at 154 eV. These ion irradiation-induced changes in the thin film stress state are in good agreement with density functional theory simulations. Furthermore, the measured elastic moduli of (V,Al)N thin films exhibit no significant dependence on E_k. The apparent independence of the elastic modulus on E_k can be rationalized by considering the concurrent and balancing effects of bombardment-induced formation of Frenkel pairs (causing a decrease in elastic modulus) and evolution of compressive intrinsic stress (causing an increase in elastic modulus). Hence, the evolution of the film stresses and mechanical properties can be understood based on the complex interplay of ion irradiation-induced defect generation and annihilation.

1. Introduction

Cubic transition metal aluminum nitrides ((c-(TM,Al)N), space group $Fm\bar{3}m$, NaCl prototype structure) are commonly employed as protective coatings for forming and cutting applications due to their superior oxidation resistance [1,2], high thermal stability [3], high hardness and elasticity [4,5], and low wear [2]. In addition to (Ti,Al)N [6,7] and (Cr,Al)N [4,8] thin films, which were in focus for many years, the phase formation and mechanical properties of (V,Al)N have recently been investigated. An exceptionally high Al solubility of $x = 0.75$ [9] in the cubic structure of $V_{1-x}Al_xN$, a larger fracture toughness in comparison to c-(Ti,Al)N [10], and a higher calculated elastic modulus of $E = 482$-492 GPa [11] for $x = 0.5$ at 0 K in comparison to $Ti_{0.5}Al_{0.5}N$ with $E = 463$-472 GPa [12] and $Cr_{0.5}Al_{0.5}N$ with $E = 373$-383 GPa [4], make c-(V,Al)N a promising protective coating material. The advanced properties of these thin films are enabled by the formation of cubic metastable solid solutions, which require non-equilibrium processing routes such as cathodic arc evaporation and magnetron sputtering.

In 1999, high power pulsed magnetron sputtering (HPPMS) technique was introduced [13]. HPPMS is characterized by a high fraction of ionized sputtered film-forming species [14], while in conventional direct-current magnetron sputtering (DCMS), the film-forming species are primarily neutrals [15].

The influence of the noble gas ion bombardment of the growing film surfaces during DCMS depositions has been reviewed with respect to enhancement of the film density [16,17], improvement of the film crystallinity, and control of the preferred orientation through collisionally-enhanced adatom mobility [18,19]. Despite the desired film densification, bombardment of the DCMS films by noble gas ions often results in trapped noble gas atoms [20] and

* Corresponding author.
E-mail address: karimi@mch.rwth-aachen.de (S. Karimi Aghda).

https://doi.org/10.1016/j.actamat.2021.117003

generation of other defects such as point defects [21,22]. During HPPMS, the high ionization degree enables control over the kinetic energy (E_k) of the noble gas as well as the film-forming ions, which results in more efficient transfer of kinetic energy and momentum to the growing film [23]. This advantage of the HPPMS process was explored during hybrid co-sputtering by means of a synchronized substrate bias potential to the metal-ion-rich portion of each HPPMS pulse which allows for the intentional separation of film-forming material fluxes originating from DCMS and HPPMS sources in time and energy domains. Specifically, Greczynski *et al.* [9] utilized a hybrid co-sputtering strategy for the growth of $V_{1-x}Al_xN$, in which the Al target was operated in HPPMS mode, while the V target was powered by a DCMS generator (Al-HPPMS/V-DCMS). By applying the substrate bias potential to the Al-rich portion of the HPPMS plasma, an unprecedented Al solubility of $x = 0.75$ was obtained. The Al solubility in this processing strategy was 42% higher than in the case of DCMS co-sputtering with a continuous direct-current substrate bias potential [9]. This exceptional Al supersaturation was achieved by stabilization of the cubic phase due to irradiation-induced stress generation [24] and more importantly by subplantaion of the Al^+ ions with energies higher than the lattice displacement threshold [9,23]. Later, it was shown that the maximum Al solubility is directly affected by the magnitude of the synchronized substrate bias potential, which defines the kinetic energy of incident Al^+ ions and consequently the subplantation depth [25].

It is reasonable to expect that the kinetic energy of ions irradiating the growing film surface defines the defect structure and, hence, also mechanical properties of the nitride thin films. Pertaining to the bond strength, it has been predicted that the elastic modulus of c-(V,Al)N depends not only on the chemical composition, but also on the defect structure and material stress state [26]. Stress-dependent elastic moduli have also been demonstrated for the isostructural c-$Cr_{0.8}Al_{0.2}N$ [27] and c-$Ti_{0.53}Al_{0.47}N$ [28].

In many studies, formation of compressive intrinsic stress is found to be related to the point defect generation during the collision cascade between the irradiating ions and atoms within the near-surface region of the growing film [29-31]. The point defect generation is assumed to be due to the displacement of the surface and subsurface atoms into interstitial and/or substitutional sites resulting in the formation of vacancies. Vacancies, which accommodate the films' off-stoichiometry, are the most discussed point defect type in cubic transition metal nitrides (c-TMN) and c-(TM,Al)N which have an influence on the thermal stability [3,32-34], elastic properties [35], and fracture behavior [36] of these thin films. The formation of off-stoichiometry vacancies is mostly correlated with the nitrogen partial pressure during the sputter deposition process [3,32], while the impact of ion irradiation is often omitted. Although ion irradiation-induced defect formation has been discussed in the literature [22,31,37], very little is known about the nature of point defects and defect clusters generated during the interaction of plasma with the growing film surface and how these defects contribute to the stress state evolution.

Density functional theory (DFT) based molecular dynamics (MD) simulations have been shown to assist the interpretation of the underlying plasma-surface interactions [38]. However, it is challenging to consider the influence of ion irradiation on the defect formation directly in DFT-based MD simulations, as ion energies above a certain threshold interfere with the periodic boundary conditions [39]. Furthermore, due to the limited dissipation of energy in the rather small supercells considered in DFT-based MD simulations [40], experimentally relevant kinetic energies of a few tens to hundreds of eV could not be treated previously. Recently, Music *et al.* [27] developed a theoretical approach, known as DFT based thermal spike model, to explicitly take into account ion irradiation with $E_k > 100$ eV and its influence on the final defect structure, density, thermally induced stress state, and elastic properties. The model has been validated experimentally for c-$Cr_{0.8}Al_{0.2}N$ [27].

Here, we systematically investigate the influence of the kinetic energy of ionized species on the structure evolution and, consequently, on the mechanical properties of c-(V,Al)N thin films by correlating experiments and *ab initio* calculations. The input data for this combined plasma-surface model are the initial ion kinetic energies, which are obtained experimentally from the ion energy distribution functions (IEDFs). Then, the total ion kinetic energy was estimated by considering in addition to the initial kinetic ion energy, also, the energy gain due to acceleration by the electric field of the substrate sheath as determined by the applied substrate bias potential. The results reveal that ion irradiation-induced formation and annihilation of point defects define the stress state evolution and the elasticity of c-(V,Al)N. Hence, thermally- as well as ion bombardment-induced stress contributions are explicitly considered here.

2. Experimental details

(V,Al)N thin films were deposited by HPPMS in an industrial scale CemeCon CC 800/9 (Würselen, Germany) deposition system with utilization of two Melec SIPP2000USB-10-500-S pulsers and 10 kW ADL GX 100/1000 DC power supplies. Two rectangular magnetrons with one composite $V_{0.6}Al_{0.4}$ target (> 99.7% purity, Plansee Composite Materials GmbH, Germany) and one elemental Al target (99.99% purity, CemeCon AG, Germany) with dimensions 8.8 × 50 cm^2 were used for the depositions in a co-sputtering geometry. 10 × 10 mm^2 Si(001) and α-Al_2O_3(0001) substrates were mounted on a copper holder facing the targets. The angles between the targets and substrate normals were ~27° and the target-to-substrate distance was 10 cm. The substrate temperature (T_s) was kept at ~450°C during all depositions. The chamber base pressure at the deposition temperature was below 0.70 mPa. A total pressure of 0.44 Pa was employed for sputtering with a constant Ar:N_2 flow rate ratio of 2:1. Each target was operated by separate HPPMS power supplies, each using pulse on-time of $\tau_{HPPMS} = 50$ μs at a duty cycle of 2.5% corresponding to a pulsing frequency of $f = 500$ Hz. Time-average powers of 2200 W for the $V_{0.6}Al_{0.4}$ target and 2000 W for the Al target were used, which resulted in the peak power densities of 520 and 490 W/cm^2, respectively. The HPPMS pulses were simultaneously applied to both targets at t = 0 μs, see Fig. 1. A pulsed substrate bias potential V_s was varied in the range from 0 (grounded) to -150 V with a pulse on-time of $\tau_s = 100$ μs synchronized with the targets' HPPMS pulses with +30 μs phase shift. The substrate bias phase shift was calculated considering the formation time of metal ions within each HPPMS pulse and the time of flight of the ions from the target to the substrate. This phase shift thus prevents acceleration of the gas ions generated at the beginning of the HPPMS pulses which may cause delamination of the deposited thin film due to detrimental stress evolution [9]. Except for the deposition, during which the substrates were kept at 0 V (grounded) throughout the experiment, the substrates were kept electrically floating at V_f = -20 V between the HPPMS pulses as measured with a digital oscilloscope. The deposition time was 120 min resulting in 2.2-2.5 μm thick films, which were used for microstructural and mechanical characterization. In addition, a set of samples was deposited under the same conditions for 3 min leading to a thickness of ~ 70 nm for mass density measurements.

An energy-resolved mass spectrometer (PPM 422, Pfeiffer Vacuum, Asslar, Germany) was employed to monitor the plasma chemistry through a mass-to-charge scan at a fixed energy, and the time-averaged IEDFs were obtained through energy scans at fixed mass-to-charge ratios of the most dominant positive ions. The measurements were carried out at the same deposition conditions

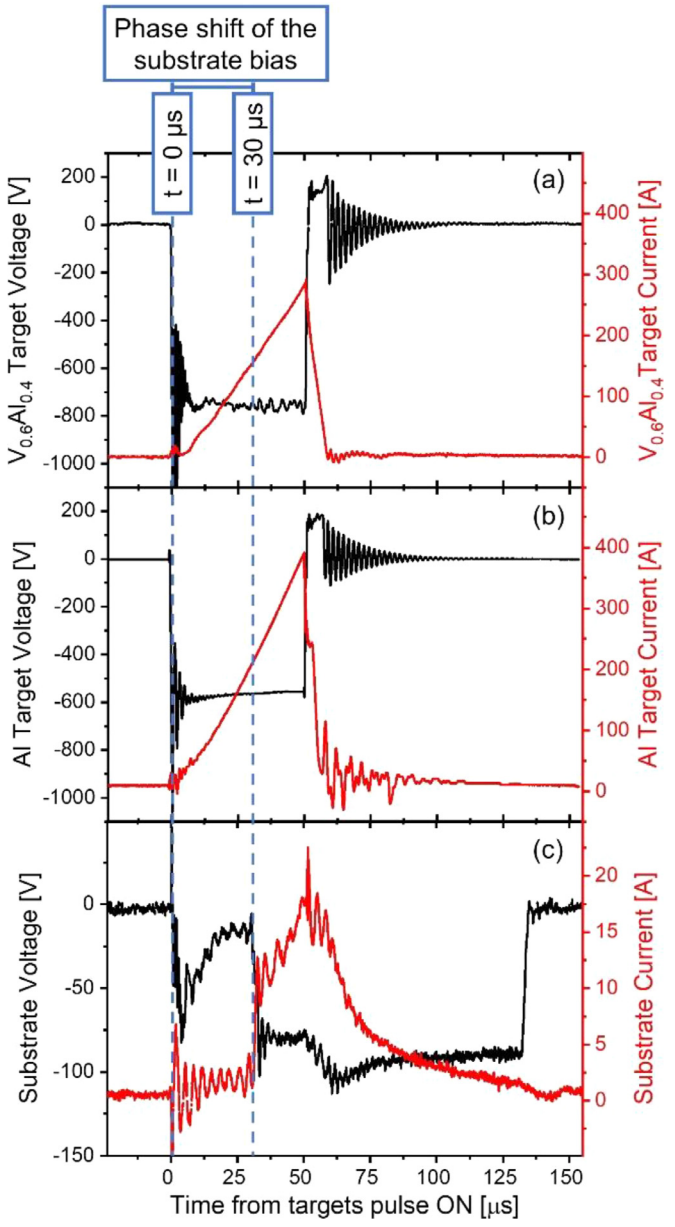

Fig. 1. Voltage and current waveforms of (a) $V_{0.6}Al_{0.4}$ and (b) Al targets recorded during the 50-µs-long HPPMS discharges. (c) Substrate voltage and substrate current waveforms at -100 V substrate bias potential.

utilized for the growth of the (V,Al)N thin films without heating. The spectrometer orifice was grounded.

Depth-resolved chemical composition analysis of the thin films grown on Si(001) was carried out by time-of-flight elastic recoil detection analysis at the Tandem Laboratory of Uppsala University. 36 MeV $^{127}I^{8+}$ primary ions were used and the incidence, as well as exit angles, were 22.5° with respect to the surface of the thin films. The solid-state detection system was located at 45° with respect to the primary ions and further details are available elsewhere [41]. Total systematic uncertainties were 2.5 at.% for N and aliquot fractions for V and Al [42]. Depth profiles were obtained from time-energy coincidence spectra by using the CONTES code [43]. Average chemical compositions of thin films grown on α-Al_2O_3(0001) were obtained by energy dispersive X-ray spectroscopy (EDX) using a JEOL JSM-6480 scanning electron microscope with an EDAX Genesis 2000 detection system at 12 kV acceleration voltage. A thin film analyzed by elastic recoil detection served as a standard for calibration of the EDX system.

Structural analyses were performed by a Siemens D5000 X-ray diffraction (XRD) system (Munich, Germany) using Cu Kα radiation source operating at a voltage and current of 40 kV and 40 mA, respectively. X-ray source and detector were coupled in θ-2θ scans (Bragg-Brentano geometry) from 30° to 70° with a step size of 0.05° and a dwell time of 2 s per step.

The thin film microstructure was characterized using scanning transmission electron microscopy (STEM). Cross-sectional and plan-view thin film lamellae were prepared by focused ion beam techniques in an FEI Helios Nanolab 660 dual-beam microscope (Hillsboro, OR, USA). This microscope was also used for acquiring bright field (BF) images with a STEM III detector at acceleration voltage and current of 30 kV and 50 pA, respectively.

Transmission electron microscopy (TEM) analyses were performed using a probe C_s-corrected FEI Titan^3 G2 60-300 (Hillsboro, OR, USA) operating at 300 kV accelerating voltage. BF-TEM images and selected area electron diffraction (SAED) patterns for the cross-sectional and plan-views of the samples were acquired using a Gatan CCD camera (Gatan Inc., Pleasanton, CA, USA).

Roughness values R_a of the thin film surfaces were evaluated with a Keyence VK-9700 laser optical microscope (Osaka, Japan).

X-ray reflectivity (XRR) measurements were carried out with a Rigaku Ultima IV diffractometer (Tokyo, Japan) using Cu radiation source at 40 kV and 40 mA in a parallel beam geometry. The XRR patterns were obtained with a step size of 0.002° and a scan speed of 0.25°/min. XRR data analysis was conducted with the Globalfit software [44].

X-ray stress analysis was done by the $sin^2\psi$ method with a Bruker D8 Discover General Area Diffraction Detection System (Billerica, MA, USA) using psi geometry (ψ tilt axis in the diffraction plane) and assuming a biaxial stress state [45]. ψ was varied from 0 to 60° corresponding to $sin^2\psi$ from 0 to 0.75. The residual stress state $\sigma_{residual}$ is determined by a least-square fit of the slope of d_ψ vs. $sin^2\psi$ according to:

$$\frac{d_\psi - d_0}{d_0} = \frac{(1+\nu)}{E}\,\sigma_{residual}\,sin^2\psi \quad (1)$$

where ν is the Poisson's ratio and E is the elastic (Young's) modulus of the thin films.

The thermal stress $\sigma_{thermal}$ contribution to the total stress state arising during cooling of the samples from T_s to room temperature was estimated by:

$$\sigma_{thermal} = \Delta\alpha\Delta T\left(\frac{E}{1-\nu}\right) \quad (2)$$

in which $\Delta\alpha$ is the difference between the linear coefficient of thermal expansion of the film (8.2×10^{-6} K^{-1}, calculated in this study) and substrates (2.5×10^{-6} K^{-1} in the case of Si [46] and 5.5×10^{-6} K^{-1} for α-Al_2O_3, provided by manufacturer). The temperature decrease ΔT after cooling from T_s to room temperature was ~ 430 K for all depositions.

Elastic modulus E and nanoindentation hardness H were determined using a Hysitron (Minneapolis, MN, USA) TI-900 TriboIndenter equipped with a Berkovich geometry-diamond tip with 100 nm radius. At least 80 quasistatic indents, each with a maximum load of 8 mN, were performed, resulting in contact depths of < 5% with respect to the film thickness. The tip area function was determined with a fused silica standard. The reduced modulus was acquired from the unloading part of load-displacement curves employing the method of Oliver and Pharr [47]. The elastic moduli were then attained from the measured reduced moduli data using the compositionally-dependent Poisson's ratios calculated by Rueß *et al.* [26]. During nanoindentation of polycrystalline nanostructures, multiple grains and hence, orientations are probed upon

mechanical loading as the elastic strain field is much larger than the domain size. Therefore, the measured elastic modulus represents an average of elastically anisotropic materials.

3. Theoretical details

DFT [48] based MD together with the DFT thermal spike model [27] were utilized to investigate the interaction of plasma with $V_{0.5}Al_{0.5}N(200)$ surface. For MD simulations, the OpenMX code was employed due to its computational speed [49]. The basis functions in this code were in the form of a linear combination of localized pseudoatomic orbitals [50] and generalized gradient approximation [51]. These basis functions were generated using a confinement scheme [50,52] specified as: V5.5-s2p2d1, Al6.0-s2p2, N4.5-s2p1, and Ar5.0-s2p1. Here, V, Al, N, and Ar designate the chemical name followed by the cutoff radius (Bohr radius unit) and the last symbols define the corresponding primitive orbitals. The energy cutoff of 150 Ry was adjusted to reach a total energy precision of 10^{-6} Ry atom^{-1}. A slab model of 512 atoms in a cluster configuration [5] was constructed, where the bottom layer was kept frozen to simulate the infinitive bulk. To describe the $V_{0.5}Al_{0.5}N(200)$ surface in the slab configuration, a 10 Å thick vacuum layer was introduced. Ar atoms with E_k= 35 eV were primarily placed at atop positions at a distance of 3 Å above V, Al, and N surface sites. Due to the limitations of the DFT-based MD calculations with respect to the energy dissipation in small supercells, interaction of ions with the structures at higher E_k could not be investigated [39,40]. DFT-based MD simulations were carried out for 1000 fs with the MD step of 1 fs at 723 K (velocity scaling thermostat, canonical ensemble), corresponding to the growth temperature of (V,Al)N in this work. A fast-transient time frame of 150 fs was observed with the maximum diffusion distances for the displaced atoms, which was accompanied by thermalization. By considering the defect structure obtained from the MD simulations and using the Kinchin-Pease equation [53], $N = \frac{E_k}{2E_d}$, in which the number of point defects (N) formed within the structure is correlated to the initial kinetic energy (E_k) of the irradiating ions and the instantaneous energy (E_d), we calculate E_d = 4.8 eV for $V_{0.5}Al_{0.5}N(200)$. E_d has been shown previously to be close to the activation energy for diffusion [27,54], which is a unique value for each material system.

In order to consider the impact of ion irradiation with E_k ranging from 39 up to 233 eV, a DFT-based thermal spike model developed by Music *et al.* [27] was utilized. Firstly, 12.5% of atoms ($4 \times 4 \times 4$ of the $8 \times 8 \times 8$ atoms supercell) from the near-surface region were subjected to high thermal loads from 10000 up to 20000 K for 150 fs. Next, the displaced atoms were inserted back into the initial supercell. Then, the supercells were relaxed at 0 K and the final defect structures were utilized to estimate the initial E_k as if the supercell was exposed to ion irradiation. This was achieved by counting the number of point defects formed due to the thermal spike and E_k was then calculated based on E_d = 4.8 eV with the Kinchin-Pease equation. The final defect structures at low E_k were comparable to the configurations obtained by MD simulations, confirming the significance of the here employed approach. The defect structures were further annealed at 723 K for 300 fs to account for the thermalization tail of the MD simulation. The VESTA code was used for the atomic structure analysis [55]. Finally, full structural relaxation was performed for each configuration and the Birch-Murnaghan equation of state [56] was used to obtain the equilibrium volume. Temperature-dependent equilibrium volume (mass density), bulk moduli, and linear coefficient of thermal expansion were calculated by the Debye-Grüneisen model [57] as described elsewhere [27]. The approximation of Hill's average was used to obtain the isotropic polycrystalline bulk modulus [58,59]. The elastic moduli were then calculated from the bulk moduli using Poisson's ratio of ν = 0.218 for $V_{0.5}Al_{0.5}N$ [26] and compared to nanoindentation measurements which probe an average elastic modulus for elastically anisotropic materials. In order to obtain the stress dependence of the elastic moduli, a volume offset from the equilibrium volume was considered for each thermal spike configuration.

4. Results and discussion

4.1. Plasma analysis

First, the plasma was characterized regarding the type and the kinetic energy of the positive ions present. The time-averaged IEDFs of gaseous and film-forming species of the V-Al HPPMS discharge in an Ar and N_2 atmosphere are presented in Fig. 2 (a) and (b), respectively. The majority of the ions present in the plasma are singly-charged Ar^+, V^+, N_2^+, N^+, and Al^+ ions. It is worth mentioning that the N^+ spectrum is measured at the mass/charge ratio of 14 amu/e, which might contain some contribution of Al^{2+} ions (13.5 amu/e) close to that of N^+. In addition, a population < 10% of doubly-charged V^{2+} ions was detected. This can be rationalized by comparing the magnitudes of second ionization potentials of V (IP^2_V = 14.66 eV) and of Al (IP^2_V = 18.83 eV) with the first ionization potential of the gaseous species, Ar (IP^1_{Ar} = 15.76 eV) and N_2 ($IP^1_{N_2}$ = 15.55 eV), [60]. However, energy fluxes calculated using:

$$energy\ flux = \int (E \times IEDF(E))dE \tag{3}$$

where E is the ion energy, show ~ 6% contribution of $V^{2+}/(V^+ + V^{2+})$, while the contribution of other doubly-charged ions, Al^{2+} and Ar^{2+}, was < 2% of the overall plasma composition. Therefore, the average charge states for V and Al ions are calculated to be 1.033 and 1.030, respectively, which is very close to one. Hence, it can be learned that the here employed plasma is dominated by singly-charged ions with Ar^+ being the most abundant species.

The kinetic energy of ionized species arriving at the growing film can be expressed as:

$$E_k = E_i^\circ + qe\left(V_{pl} - V_s\right) \tag{4}$$

in which E_i° represents the initial kinetic energy of the ions prior to entering the substrate sheath. While the kinetic energy gained from the acceleration across the substrate sheath is $qe(V_{pl} - V_s)$, where q denotes the ion charge state, e is the elementary charge, V_{pl} is the plasma potential, and V_s is the negative substrate bias potential. Hence, the magnitude of E_k is primarily affected by the substrate bias potential. All IEDFs (measured with respect to ground (V_s = 0 V)) exhibit a most probable energy of ~ 4 ± 1 eV corresponding to 89% of the total ion population, see Fig. 2. For the gaseous species, Ar^+ and N_2^+, considering $E_i^\circ \sim 0eV$, the measured most probable energy of the IEDFs corresponds numerically to the plasma potential. However, for the film forming species, $E_i^\circ > 0eV$, the most probable energy of the IEDFs is shifted to slightly higher values while the IEDFs extend to energies of up to 24 eV. This energy range for the total ion population is rather small in comparison to, for example, a DCMS discharge of Hf or Zr in Ar and O_2 atmosphere, which showed IEDFs with energies extending up to 400 eV [61]. The here measured IEDFs, however, are comparable to observations in other reactive HPPMS discharges of Cr-Al [27] and non-reactive sputtering of V-Al-C [62]. The extended energetic tail can be associated with the remaining kinetic energy of the sputtered species after transport through the gas phase or it may originate from the time-variation of the plasma potential during HPPMS pulses and the subsequent acceleration of the ions over the modulated sheath potential [63]. As the most probable energy range of 4 ± 1 eV encompasses 89% of the total ion population, the from 0 (grounded) to -150 V varied substrate bias potential resulted in a most probable E_k ranging from 4 to 154 eV for singly-charged ions.

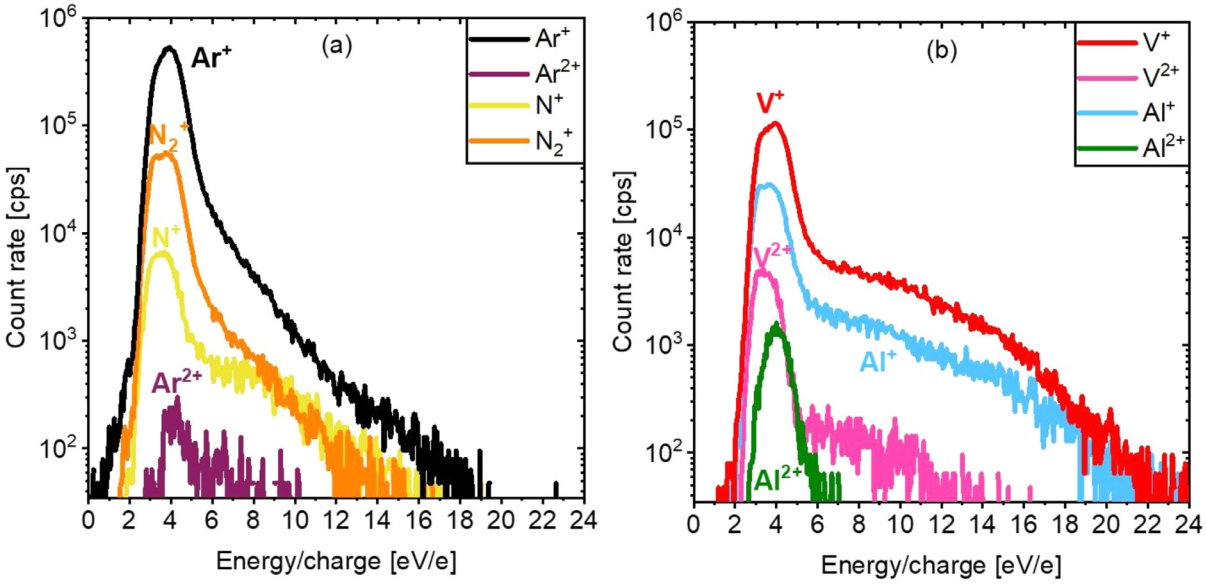

Fig. 2. Time-averaged IEDFs of (a) gaseous and (b) sputtered film-forming species, for V-Al HPPMS discharge in an Ar and N_2 atmosphere.

Considering that Ar, V, Al, N_2, and N species present in the plasma having different masses, the average mass of the ions irradiating the surface is calculated to be $m_{ave} = 40.08$ amu under the here measured plasma condition. This is very close to the mass of Ar, $m_{Ar} = 39.95$ amu. Therefore, Ar^+ ions were utilized to simulate the average momentum transfer in high energy plasma-surface interactions as mentioned in Section 3.

4.2. Film composition

Chemical composition depth profiles from thin films grown on Si (not shown) revealed homogeneous distributions of V, Al, and N for the probed depth of up to 220 nm from the surface. Table S1 of the supplementary material summarizes the chemical composition of all synthesized thin films. All films exhibited chemical compositions in the range of 20.7 to 23.5 at.% for V, 25.7 to 27.2 at.% for Al, and 50.8 to 52.0 at.% for N were obtained and the maximum statistic uncertainty was < 0.4 at.%, while the sum of Ar and O impurities was < 1 at.%. According to predictions by Rueß *et al.* [26], the maximum nitrogen content of 52 at.% changes the elastic modulus of $(V_{0.5}Al_{0.5})_{1-y}N_y$ below 5 GPa with respect to the elastic modulus of stoichiometric composition. Therefore, the here obtained composition-induced change in elastic modulus is with 1.1% significantly lower than the stress-induced changes of up to 7.4% when comparing stress states of -4 and 0 GPa. Thus, while the stress-induced change in elastic modulus is significant, the chemical composition differences affect the elasticity only marginally. Based on the data presented in Table S1, an average film composition of $(V_{0.46\pm0.01}Al_{0.54\pm0.01})_{0.49\pm0.02}N_{0.51\pm0.02}$. can be calculated. For the remaining discussion the more concise composition description of $(V_{0.46}Al_{0.54})_{0.49}N_{0.51}$ is used.

4.3. Structural analysis

The phase formation of thin films grown with different ion kinetic energy was probed by XRD and is shown in Fig. 3 for (a) Si(001) and (b) α-Al_2O_3(0001) substrates.

The diffractograms reveal the formation of a single phase metastable cubic $(V_{0.46}Al_{0.54})_{0.49}N_{0.51}$ solid solution, independent of E_k and the substrate material. No evidence for the presence of secondary phases, e.g. hexagonal AlN [64], was obtained. At $E_k = 4$ eV, films with (111) preferred orientation are observed. As the substrate bias potential and hence E_k is increased, the intensity of the (111) diffraction peak reduces and a close to random orientation is observed at $E_k = 74$ and 104 eV. The (200) peak intensity reaches a maximum at $E_k = 154$ eV. Furthermore, the cross-sectional and plan-view SAED patterns of low and high energy-deposited films (Figure S1 of the supplementary material) reveal, consistent with XRD data, the formation of a single-phase cubic structure. Furthermore, the XRD shown in Fig. 3, and the cross-sectional SAED patterns presented in Figure S1 (a), (b), and (c) indicate the change in preferred orientation from (111) to (100) as $E_k = 4$ eV is increased to $E_k \geq 104$ eV. The evolution of the preferred orientation can be understood by comparing the surface energies of corresponding planes. In the case of isostructural $Ti_{0.50}Al_{0.50}N$, Forslund *et al.* [65] have theoretically obtained the surface energies (E_{surf}) of the (100) plane, $E_{surf}^{(100)} = 1.34$ J/m^2, (110) plane, $E_{surf}^{(110)} = 3.39$ J/m^2 (unrelaxed supercell), and (111) plane, $E_{surf}^{(111)} = 4.20$ J/m^2. During growth under relatively low mobility condition, $E_k = 4$ eV, adatoms have a higher probability to be incorporated into the high energy and low diffusivity (111) surface than in the low energy (high diffusivity) planes resulting in the kinetically limited, upward growth of (111) planes. However, as the ion kinetic energy is increased to $E_k > 74$ eV, enhanced adatom mobility favors the incorporation of adatoms into the low energy (200) surface in addition to the high energy (111) surface. These observations are also consistent with the preferred orientation evolution reported for the ion assisted growth of isostructural binary TiN, ScN and VN thin films [66-69].

4.4. Morphological evolution

Next, the influence of E_k on the morphology of $(V_{0.46}Al_{0.54})_{0.49}N_{0.51}$ thin films is probed by cross-sectional and plan-view BF-STEM, see Fig. 4.

Thin films deposited with low $E_k \leq 24$ eV exhibit a pronounced coarse-grained columnar morphology with an average column width of 100 ± 20 nm (Fig. 4 (a), (b), (f), and (g)) elongated along the growth direction. The conditions are corresponding to low-temperature, low-energy ion irradiation [17], in which the limited nucleation rate promotes competitive columnar growth. In addition, limited surface diffusion may cause formation of underdense regions at the grain boundaries. At $E_k \geq 74$ eV, formation of

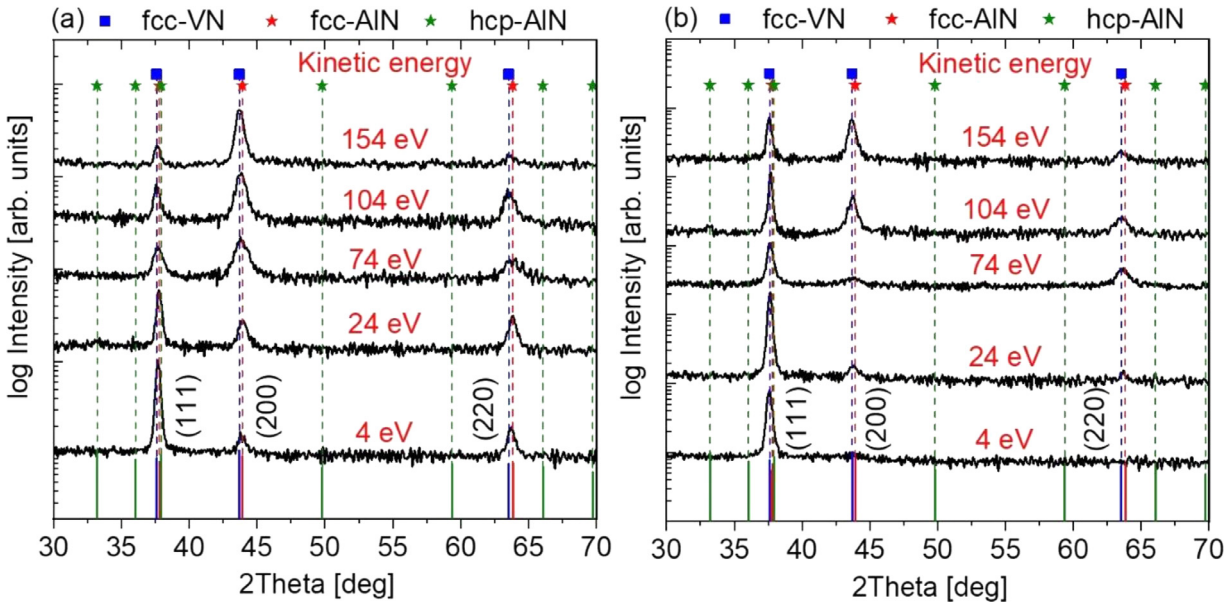

Fig. 3. Structure evolution of $(V_{0.46}Al_{0.54})_{0.49}N_{0.51}$ thin films deposited on (a) Si(001) and (b) α-Al_2O_3(0001) substrates, for different kinetic energy of ionized species.

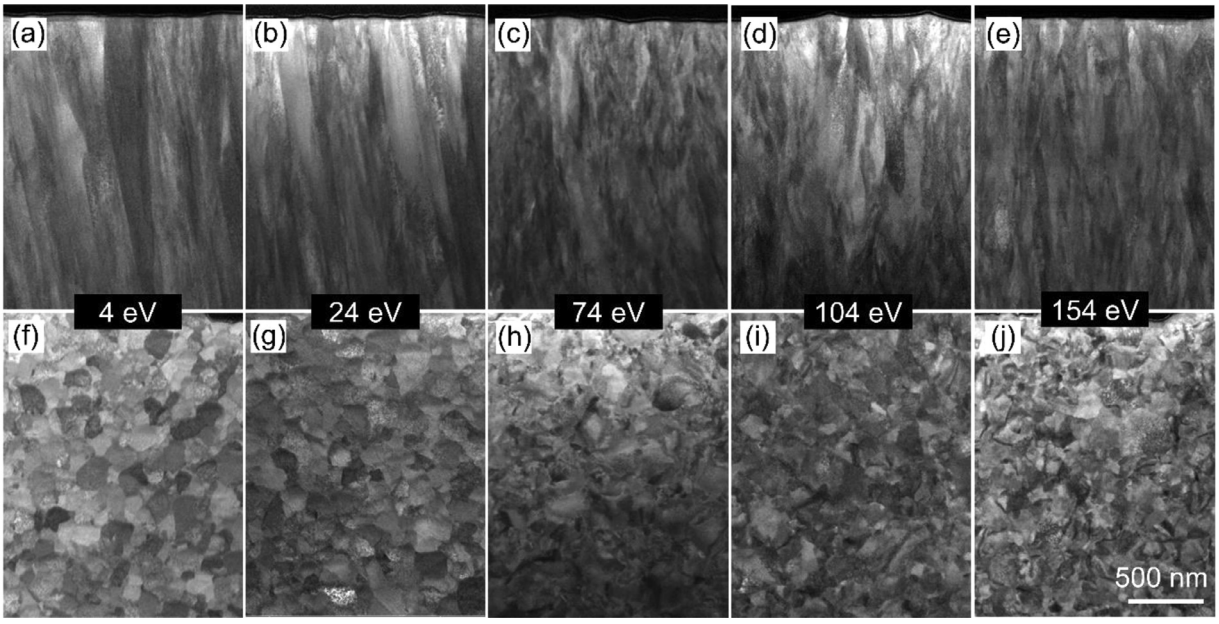

Fig. 4. Cross-sectional (top) and plan-view (bottom) BF-STEM images of $(V_{0.46}Al_{0.54})_{0.49}N_{0.51}$ deposited on Si with ion kinetic energies of (a) and (f) 4 eV, (b) and (g) 24 eV, (c) and (h) 74 eV, (d) and (i) 104 eV, (e) and (j) 154 eV. The scale bar in (j) is valid for all the micrographs.

a fine-grained microstructure is observed (Fig. 4 (c) – (e) and (h) – (j)). The evolution of fine-grained nanocrystalline structure under ion irradiation with $E_k \geq 74$ eV is consistent with the extended structure zone diagram proposed by Anders [70] and may be rationalized by ion irradiation-induced defect formation resulting in renucleation.

Although significant ion irradiation-induced alterations in morphology were observed, the X-ray reflectivity (XRR) data presented in Figure S2 of the supplementary material revealed a comparable mass density of 4.86 ± 0.08 and 4.88 ± 0.06 g/cm^3 for thin films deposited with $E_k = 24$ and 104 eV, respectively. However, it has to be considered that XRR was performed on a set of very thin samples (~ 70 nm) grown under identical conditions as the films with a thickness > 2 μm in order to minimize surface roughness, which would otherwise hamper the reflection of the X-ray beam. To investigate the morphological evolution as a function of the film thickness, TEM was carried out for the thin films grown with $E_k = 24$ and 104 eV. The micrographs presented in Fig. 5 show the initial growth at the substrate ((a) 24 eV, (b) 104 eV) and the near-surface regions ((c) 24 eV, (d) 104 eV).

The cross-sectional BF-TEM images in Fig. 5 (a) and (b) reveal similar growth initiation pathways (first 100 nm) independent of E_k as indicated by the blue dashed rectangles. However, at a thickness of ~ 500 nm, the ion energy-induced differences in morphology are evident. At $E_k = 24$ eV competitive columnar grain growth with inter-columnar pores, apparent from the white regions in the columnar grain boundaries as marked by the orange arrows, are formed. It is reasonable to assume that this is due to limited adatom mobility [17]. A clear indication of the pores was observed in plan-view TEM micrograph from the near-surface re-

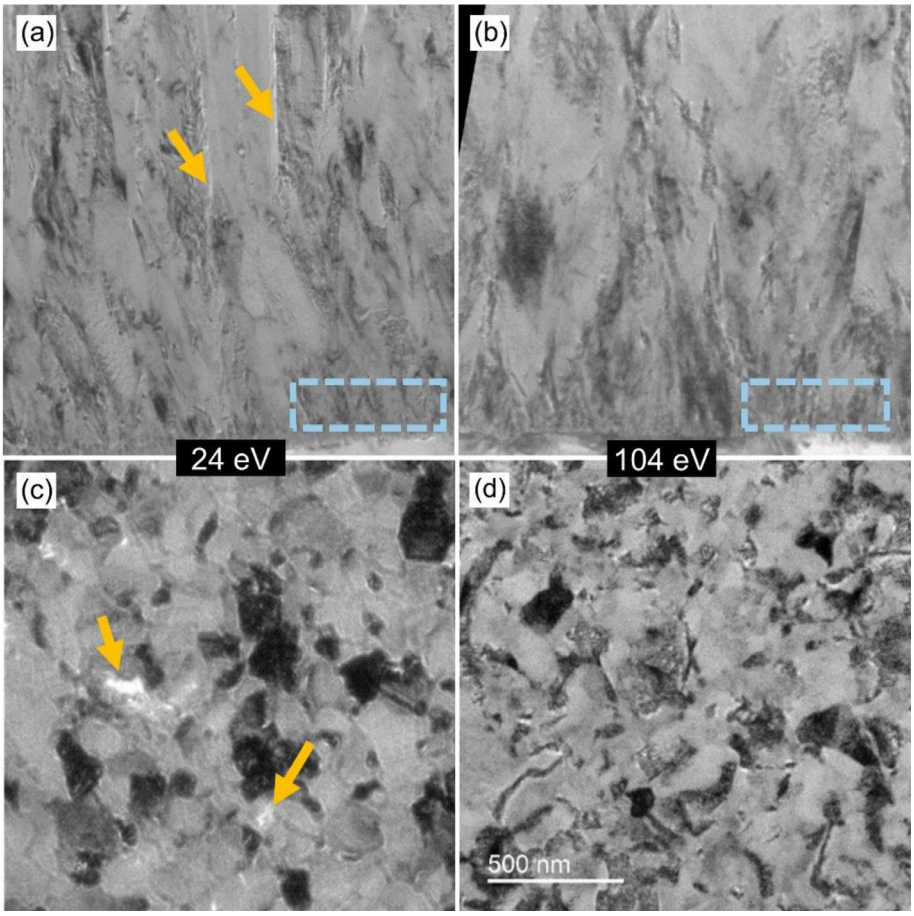

Fig. 5. Cross-sectional (top) and plan-view (bottom) TEM micrographs of $(V_{0.46}Al_{0.54})_{0.49}N_{0.51}$ deposited on Si with ion kinetic energies of (a) and (c) 24 eV and (b) and (d) 104 eV, respectively. The blue dashed rectangles show the near substrate regions and the orange arrows depict the pores at near-surface regions. The scale bar in (d) is valid for all the micrographs.

gion of the thin film with $E_k = 24$ eV in Fig. 5 (c) as marked by orange arrows. It can reasonably be expected that such porous intercolumnar regions lead to a reduction in the overall mass density of the low energy deposited films, which could not be verified by XRR measurements on the ~ 70 nm thick films. The faceted columnar growth observed in films deposited at low energy of $E_k = 24$ eV results in surface roughness value of $R_a = 42 \pm 6$ nm. Therefore, it is reasonable to assume that atomic shadowing induced by surface roughness leads to the formation of underdense regions at the grain boundaries [17]. In contrast, at $E_k = 104$ eV, the enhanced adatom mobility leads to a reduction of surface roughness by 55% to $R_a = 18 \pm 6$ nm and hence, growth of a fine-grained morphology with dense grain boundaries (Fig. 5 (d)).

4.6. Mechanical properties

Ion irradiation-induced densification is often accompanied by generation of compressive residual stresses with reported values of up to -9.1 GPa [71]. The consequences of variation in the E_k on the residual stress state are presented in Fig. 6 (a). The obtained thermal stress contributions ($\sigma_{thermal}$) to the overall residual stresses at $\Delta T = 430$ K are +1.4 and +0.6 GPa for $(V_{0.46}Al_{0.54})_{0.49}N_{0.51}$ thin films deposited on Si and α-Al_2O_3, respectively. For films grown at $E_k = 4$ eV, a tensile residual stress of 0.3 ± 0.2 GPa and a compressive residual stress of -1.1 ± 0.2 GPa for the films deposited on Si and α-Al_2O_3, respectively, were obtained. The substrate material induced-differences between $\sigma_{residual}$ appear to be due to the differences in the $\sigma_{thermal}$ values, which originate from the differences in the linear thermal expansion coefficients of the Si (2.5×10^{-6} K^{-1}) and α-Al_2O_3 (5.5×10^{-6} K^{-1}) substrates and the thin films (8.2×10^{-6} K^{-1}). For higher E_k, a significant increase in compressive stress was measured up to a maximum of -3.3 ± 0.4 and -4.2 ± 0.4 GPa at $E_k = 104$ eV for the films deposited on Si and α-Al_2O_3, respectively. For even higher E_k, stress relaxation occurred as compressive residual stress is reduced by 61% and 55% for the films deposited on Si and α-Al_2O_3, respectively.

The elastic modulus values are shown as a function of E_k in Fig. 6 (b). They vary marginally from 440 to 431 GPa and from 462 to 445 GPa for the films deposited on Si and α-Al_2O_3, respectively. Thin films deposited on the α-Al_2O_3 substrate exhibit up to 25 GPa higher values of the elastic modulus in comparison to the films grown on Si. This increase might partially be rationalized based on the difference between the measured residual stress state of films deposited on Si and α-Al_2O_3 of up to 1.5 GPa. This stress state difference corresponds to ~15 GPa difference in elastic modulus as calculated theoretically by Rueß *et al.* [26]. Hence, the difference in the thermal residual stress state caused the enhancement of elasticity of the films grown on α-Al_2O_3. A stress-dependent elasticity was also demonstrated for $Cr_{0.8}Al_{0.2}N$ [27] and $Ti_{0.53}Al_{0.47}N$ [28] experimentally as well as by DFT simulations. Furthermore, no significant change in the elastic modulus can be observed for the $(V_{0.46}Al_{0.54})_{0.49}N_{0.51}$ thin films deposited at various E_k regardless of their residual stress state, Fig. 6 (a) and (b). This is in contrast to the stress induced-elasticity calculations by Rueß *et al.* [26]. Additionally, an increase of ~ 12% in indentation hardness was observed, independently of the substrate material, as E_k is increased

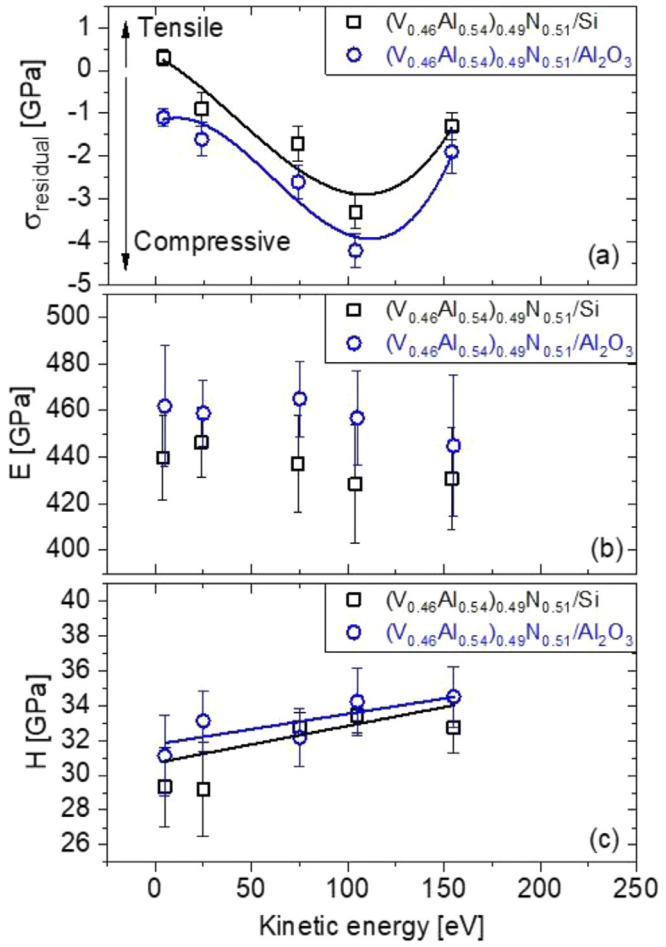

Fig. 6. (a) Residual stress ($\sigma_{residual}$), (b) elastic modulus (E), and (c) nanoindentation hardness (H) as a function of ion kinetic energy, obtained from thin films deposited on Si and α-Al_2O_3 substrates.

from 4 to 154 eV, Fig. 6 (c). The slight increase in hardness might be attributed to the evolution of a fine-grained structure and residual compressive stress state in the thin films at higher ion kinetic energies [72].

4.7. DFT-based thermal spike model

In order to understand the above-discussed discrepancy between theory [26] and experiment, a DFT-based thermal spike model was utilized to mimic the ion irradiation effect at the atomistic scale. It has to be mentioned that the model describes exclusively ion irradiation effects and does not include the growth-related mechanisms such as renucleation and morphological alteration, which are observed experimentally. Ar^+ ions were utilized here to simulate the average momentum transfer in high energy plasma-surface interactions. The nominal theoretical composition of $V_{0.5}Al_{0.5}N$ was chosen to represent the average film composition of $(V_{0.46}Al_{0.54})_{0.49}N_{0.51}$.

Fig. 7 exhibits the final $V_{0.5}Al_{0.5}N(200)$ atomic configurations after thermal spikes, representing E_k up to 233 eV. Firstly, the dissipation of the primary energy from irradiation provides the required activation energy for not only surface but also sub-surface diffusion of the atoms. This observation is consistent with the notion of irradiation (subplantation)-induced sub-surface diffusion in c-(V,Al)N, which has been argued to be enabled experimentally by controlling the ion energy of irradiating species above the lattice displacement threshold [9]. It is also evident from Fig. 7 that the activation of sub-surface diffusion, consequently, leads to formation of self-interstitial/vacancy point-defect pairs (Frenkel pairs), which remain frozen within the structure. Formation of Frenkel pairs has also been discussed in the case of isostructural TiN [54] and $Cr_{0.8}Al_{0.2}N$ [27]. The increase in E_k is accompanied by an increase in the population of point defects, Fig. 7. However, above a certain threshold of input ion energy, $E_k > 165$ eV, a great number of surface atoms gain enough mobility leading to resputtering and amorphization of the near-surface regions. Mobility of the species above the lattice displacement threshold from the surface is observed not only for the N atoms but also for Al and V species forming different vacancy sites. In addition, the largest thermal spike employed, representing an ion irradiation energy of $E_k = 233$ eV, seems to promote defect annihilation as the surface of the supercell is partially recovered as indicated by the orange dashed square in the corresponding configuration in Fig. 7.

The defect structures (Fig. 7) explicitly consider the ion irradiation effects, which are expected to determine the ground-state properties of c-$V_{0.5}Al_{0.5}N$. The calculated lattice parameters as a function of E_k are compared to the experimentally measured values from the (200) lattice plane in Fig. 8 (a). When the ion energy is increased from 0 to 165 eV, an increase in the predicted lattice parameter values from 4.114 to 4.139 Å is observed. Higher ion kinetic energy of 233 eV, however, results in a reduction of lattice parameter to 4.126 Å. Although a slight deviation of below 0.4% is obtained between the absolute values at $E_k \sim 0$ eV, there is an excellent agreement between theoretical and experimental lattice parameter evolution of (V,Al)N with respect to E_k. It is important to mention that the *ab initio* calculations corresponding to $E_k \sim 0$ eV are performed on an ideal structure (single crystal) without presence of any defects. However, the experimentally obtained polycrystalline thin films, even at low ion kinetic energies ($E_k = 4$ eV), contain microstructural defects such as pores and grain boundaries which were not considered in the DFT-based model.

The resulting evolution of the lattice parameter is associated with the generation of intrinsic stresses as shown in Fig. 8 (b). Here, the theoretical intrinsic stress corresponding to each defect structure is calculated by considering the ion kinetic energy-induced volume change with respect to the equilibrium volume of the ideal defect-free structure at $E_k = 0$ eV. The volume change is then converted into a stress value by utilizing the fitted equation of state.

The here calculated intrinsic stress states are directly connected to the generation of point defects due to ion irradiation. So far, *ab initio* based simulations which systematically consider ion energy-induced changes of the stress state have neither been reported for binary TMNs nor ternary (TM,Al)Ns. The steep increase in the theoretical intrinsic compressive stress is accompanied by stress relaxation as the E_k is increased. This trend is consistent with the experimental evolution of intrinsic stress. It should be noted that in the DFT-based thermal spike model, only point defects are considered and slight discrepancies in the absolute values of theoretically and experimentally obtained $\sigma_{intrinsic}$ might be due to other micro- and macro-stresses such as peening effects at the grain boundaries, which are not treated by DFT in this study.

Fig. 8 (c) and (d) summarize the population of Frenkel pairs (self-interstitial/vacancy pairs) and vacancies formed in $V_{0.5}Al_{0.5}N(200)$ as a function of E_k, respectively. Although, the concurrent generation of both defect types is evident, at lower kinetic energies ($E_k \leq 165$ eV), the population of Frenkel pairs is dominant over the vacancy population. Contrary, at $E_k > 165$ eV, enhancement of adatom mobility and diffusivity lead to annihilation of Frenkel defects and promote the formation of vacancies. It is evident that at 165 eV the maximum population of Frenkel pairs of around 3%, the largest lattice parameter, and the maximum in-

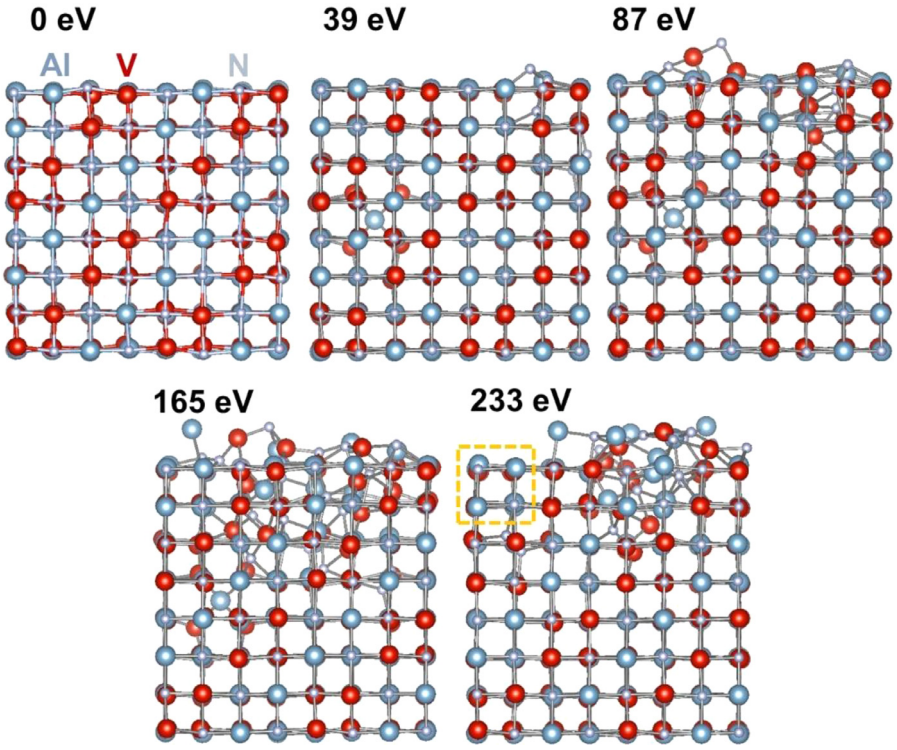

Fig. 7. Thermal spike model for $V_{0.5}Al_{0.5}N(200)$ corresponding to energetic ion irradiations. The initial kinetic energy of impinging ion E_k is shown above each final defect structure. In the defect structure with E_k = 233 eV, a dashed square (in orange) represents a recovered surface region due to defect annihilation.

Table 1
The calculated formation energies of Frenkel pairs ($E^F_{species}$) and vacancies ($E^V_{species}$) in $V_{0.5}Al_{0.5}N$.

Formation energies	Species (defect type)		
	N	Al	V
$E^F_{species}$ (eV)	6.52	6.71	7.89
$E^V_{species}$ (eV)	1.59	1.67	1.97

trinsic compressive stress is obtained. Table 1 lists the calculated formation energies of single Frenkel pairs ($E^F_{species}$) and vacancies ($E^V_{species}$).

The here presented formation energies for nitrogen point defects, E^F_N = 6.52 eV and E^V_N = 1.59 eV, are very similar to the calculated values for a nitrogen Frenkel pair [54] and vacancy [73] formation in the isostructural TiN of 7.1 and 2.4 eV, respectively. In general, the results displayed in Table 1 show lower formation energies for nitrogen point defects in comparison to the metallic point defects. This results in a factor of 2 to 5 higher populations of both, N-Frenkel pairs as well as N-vacancies, according to the here utilized thermal spike model, see Fig. 8 (c) and (d). Moreover, it can be observed that higher E_k leads also to the formation of both V and Al point defects. While the formation energies of Frenkel pairs are calculated to be higher than of the vacancies, the high E_k of tens of eV is expected to be sufficient to form Frenkel pairs as well. The dynamics of the Frenkel pair formation is also observed in the classical MD simulations for the isostructural TiN [54].

In order to disentangle the contributions of Frenkel pairs and vacancies to the lattice parameter as well as residual stress state, their relative changes caused by 0.2% point defect population (presence of one point defect in the supercells with 512 atoms) is investigated and compared to a pristine supercell with 0% point defect population. The results are summarized in Fig. 8 (e) and (f), respectively. While the presence of Frenkel pairs causes an increase in the lattice parameter with maximum of 0.2% relative change for an Al-Frenkel pair, the presence of vacancies results in a reduction of lattice parameter, with maximum of -0.08% relative change for an Al-vacancy, independent of the defect species, Fig. 8 (e). Hence, the presence of point defects causes the expansion and/or contraction of the lattice which in turn affects directly the intrinsic stresses within the structure.

The stress states generated due to the presence of 0.2% N-, Al-, and V-Frenkel pairs are -0.4, -0.7, and -0.6 GPa compressive and due to the presence of 0.2% N-, Al-, and V-vacancies are with 0.2, 0.4, and 0.4 GPa tensile, see Fig. 8 (f). By considering the population difference between the Frenkel defects and vacancies generated at each E_k, the maximum compressive stress formed in the structure at E_k = 165 eV is defined by the highest population of Frenkel pairs, Fig. 8 (d). In contrast, at E_k = 233 eV, the population of vacancies formed due to the high mobility of atoms increases at the expense of the annihilation of Frenkel pairs, which concurrently causes lattice stress relaxation. Hence, the evolution of the lattice parameter and stress state upon variation of E_k can be attributed to the formation and annihilation of different types of point defects. The correlation between the stress relief and the dynamic defect annihilation has also been discussed in the literature. Davis [74] proposed a model, in which stress relaxation was attributed to ion irradiation-induced thermal spikes. In addition, McKenzie [75] suggested that thermal spikes result in atomistic scale melting and defect annihilation thereby, enabling stress relaxation.

To evaluate the influence of irradiation induced-changes in the defect structure and stress state on the elasticity of (V,Al)N, elastic modulus was calculated for each thermal spike configuration at 300 K (near room temperature) from the Debye-Grüneisen model. The results are presented in Fig. 9. The elastic modulus of stress-free $V_{0.5}Al_{0.5}N$ at E_k= 0 eV is calculated to be 472 GPa. As E_k is increased to 165 eV, an 11% reduction in elastic modulus to 425

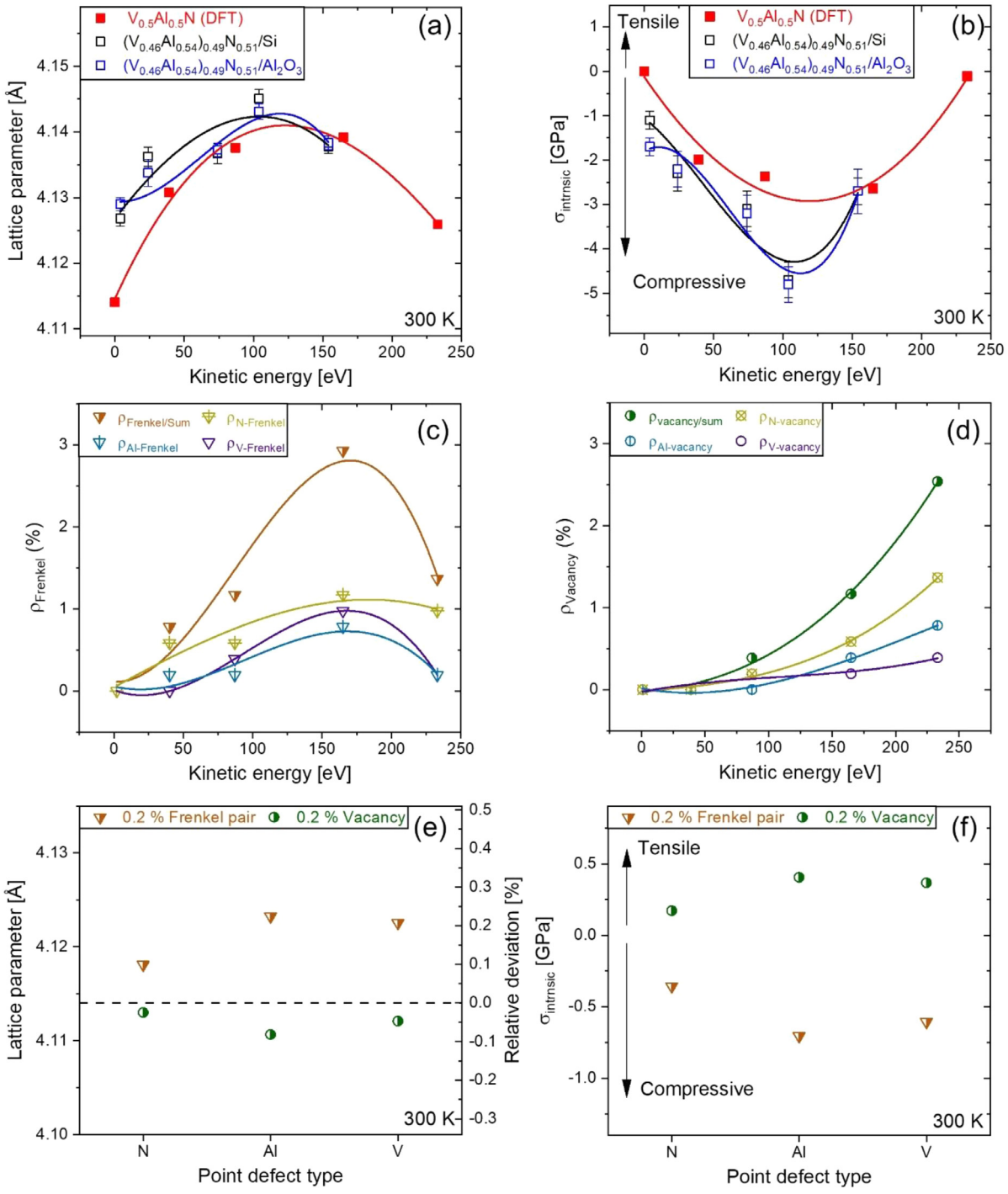

Fig. 8. Calculated and measured lattice parameter (a) and intrinsic stress (b) of (V,Al)N with respect to the ion kinetic energy. Population of Frenkel pairs (c) and vacancies (d) from the DFT thermal spike model with respect to the ion kinetic energy. Calculated lattice parameters (e) and intrinsic stresses (f) in the presence of 0.2% lattice defects.

GPa is obtained, which converges to 427 GPa at E_k= 233 eV. This significant reduction in elastic modulus is associated with the generation and population of point defects.

Moreover, according to Rueß *et al.* [26], the presence of -2 GPa compressive stress increases the predicted elastic modulus by ~ 18 GPa, hence, an increase by 4% independent of E_k. Enhancement of the elasticity due to presence of compressive stress is attributed to the pressure-induced bond strengthening [26,27,76,77]. For comparison, the experimentally determined elastic moduli of $(V_{0.46}Al_{0.54})_{0.49}N_{0.51}$ thin films deposited on Si and α-Al_2O_3 substrates are also shown in Fig. 9. While thin films deposited at different kinetic energies exhibit structural and stress state alterations, the elastic moduli show no significant dependence on E_k.

Ab initio simulations reveal that the measured elastic modulus, which is apparently unaffected (within the measurement error) by changes in the ion kinetic energy, can be rationalized by the concurrent ion irradiation-induced point defect formation (causing a decrease in elastic modulus) and compressive stress generation (causing an increase in elastic modulus). At E_k= 4 eV, the measured elastic moduli show ~8% - 10% lower values in comparison to the calculated elasticity data, which can readily be explained by the experimentally verified (see Fig. 5) presence of pores induced by limited adatom mobility during growth of the films. Besides the

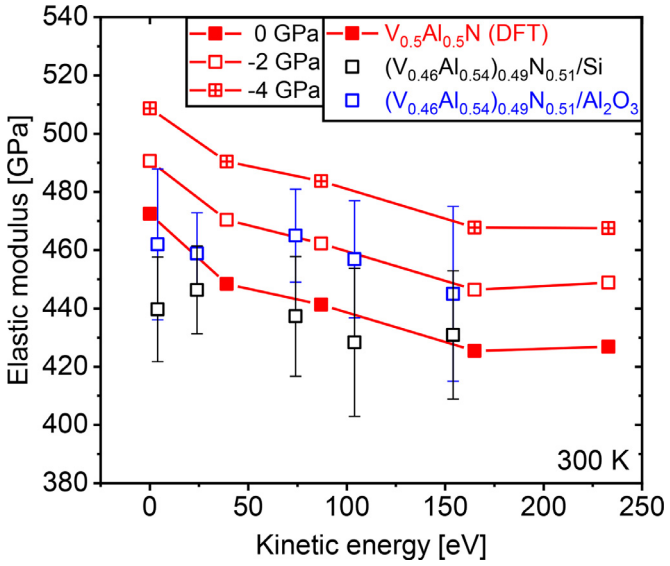

Fig. 9. Calculated and measured elastic moduli of (V,Al)N as a function of ion kinetic energy.

slight deviation at low E_k, there is a very good agreement between the experimentally measured and predicted elasticities for the remaining ion kinetic energy range.

5. Conclusions

The influence of the ion kinetic energy (E_k) on the structure evolution and mechanical properties of (V,Al)N layers deposited by HPPMS has been systematically investigated by correlation of experiments and DFT simulations. Single-phase cubic $(V_{0.46}Al_{0.54})_{0.49}N_{0.51}$ films were grown on both Si and α-Al_2O_3 substrates in the E_k range from 4 to 154 eV. At low $E_k \leq 24$ eV, an underdense microstructure with columnar grains, preferred (111) orientation, and low intrinsic stress state of -1.1 GPa was observed. Increasing the E_k to 104 eV resulted in the evolution of a fine-grained structure, free of pores. Concurrent with the ion irradiation-induced densification, which was revealed by TEM micrographs, a significant increase in compressive intrinsic stress up to a maximum value of -4.8 GPa at 104 eV was measured, followed by an ion irradiation-generated stress relaxation to -2.7 GPa at 154 eV. Excellent agreement between the experimental and *ab initio* simulations of ion irradiation-induced stress state evolution was observed. In contrast to film density and residual stress state, the experimentally determined elastic modulus appears to be independent of ion energy. This unexpected behavior can be understood based on *ab initio* data: While an increase of E_k during growth of (V,Al)N thin films results in the formation of Frenkel defects (causing a decrease in elastic modulus), concomitantly also compressive stresses are generated (causing an increase in elastic modulus), resulting in an apparently ion energy independent-elastic modulus. It is evident that the evolution of film stress and mechanical properties can be rationalized based on the here presented *ab initio* data, capturing the complex interplay of ion irradiation-induced defect generation and annihilation.

Declaration of Competing interest

The authors declare that they have no known competing financial interests or personal relationships that could have appeared to influence the work reported in this paper.

Acknowledgments

This work was supported by the Leibniz Association (Collaborative Excellence Project K128/2018) as well as by Deutsche Forschungsgemeinschaft within the Collaborative Research Center SFB-TR 87/3 “Pulsed high power plasmas for the synthesis of nanostructured functional layers”. Simulations were performed with computing resources granted by JARA-HPC from RWTH Aachen University under Project JARA0151. Financial support for the operation of the accelerator laboratory in Uppsala by VR-RFI (Contract No. 2017-00646_9) and the Swedish Foundation for Strategic Research (SSF, Contract No. RIF14-0053) is gratefully acknowledged.

Supplementary materials

Supplementary material associated with this article can be found, in the online version, at doi:10.1016/j.actamat.2021.117003.

References

[1] D. McIntyre, J.E. Greene, G. Håkansson, J.E. Sundgren, W.D. Münz, Oxidation of metastable single-phase polycrystalline $Ti_{0.5}Al_{0.5}N$ films: Kinetics and mechanisms, Journal of Applied Physics 67 (3) (1990) 1542–1553.
[2] A.E. Reiter, V.H. Derflinger, B. Hanselmann, T. Bachmann, B. Sartory, Investigation of the properties of $Al_{1-x}Cr_xN$ coatings prepared by cathodic arc evaporation, Surface and Coatings Technology 200 (7) (2005) 2114–2122.
[3] M. to Baben, M. Hans, D. Primetzhofer, S. Evertz, H. Ruess, J.M. Schneider, Unprecedented thermal stability of inherently metastable titanium aluminum nitride by point defect engineering, Materials Research Letters 5 (3) (2017) 158–169.
[4] P.H. Mayrhofer, D. Music, T. Reeswinkel, H.G. Fuß, J.M. Schneider, Structure, elastic properties and phase stability of $Cr_{1-x}Al_xN$, Acta Materialia 56 (11) (2008) 2469–2475.
[5] P.H. Mayrhofer, D. Music, J.M. Schneider, Influence of the Al distribution on the structure, elastic properties, and phase stability of supersaturated $Ti_{1-x}Al_xN$, Journal of Applied Physics 100 (9) (2006) 094906.
[6] W.D. Münz, Titanium aluminum nitride films: A new alternative to TiN coatings, Journal of Vacuum Science & Technology A 4 (6) (1986) 2717–2725.
[7] D. Music, R.W. Geyer, J.M. Schneider, Recent progress and new directions in density functional theory based design of hard coatings, Surface and Coatings Technology 286 (2016) 178–190.
[8] X.-Z. Ding, X.T. Zeng, Structural, mechanical and tribological properties of CrAlN coatings deposited by reactive unbalanced magnetron sputtering, Surface and Coatings Technology 200 (5) (2005) 1372–1376.
[9] G. Greczynski, S. Mráz, M. Hans, D. Primetzhofer, J. Lu, L. Hultman, J.M. Schneider, Unprecedented Al supersaturation in single-phase rock salt structure VAlN films by Al^+ subplantation, Journal of Applied Physics 121 (17) (2017) 171907.
[10] J.S.K.L. Gibson, S. Rezaei, H. Rueß, M. Hans, D. Music, S. Wulfinghoff, J.M. Schneider, S. Reese, S. Korte-Kerzel, From quantum to continuum mechanics: studying the fracture toughness of transition metal nitrides and oxynitrides, Materials Research Letters 6 (2) (2018) 142–151.
[11] K.P. Shaha, H. Rueβ, S. Rotert, M.t. Baben, D. Music, J.M. Schneider, Nonmetal sublattice population induced defect structure in transition metal aluminum oxynitrides, Applied Physics Letters 103 (22) (2013) 221905.
[12] V. Podgursky, Ab initio calculations of elastic properties of isotropic and oriented $Ti_{1-x}Al_xN$ hard coatings, Journal of Physics D: Applied Physics 40 (13) (2007) 4021–4026.
[13] V. Kouznetsov, K. Macák, J.M. Schneider, U. Helmersson, I. Petrov, A novel pulsed magnetron sputter technique utilizing very high target power densities, Surface and Coatings Technology 122 (2) (1999) 290–293.
[14] J. Bohlmark, J. Alami, C. Christou, A.P. Ehiasarian, U. Helmersson, Ionization of sputtered metals in high power pulsed magnetron sputtering, Journal of Vacuum Science & Technology A 23 (1) (2005) 18–22.
[15] I. Petrov, A. Myers, J.E. Greene, J.R. Abelson, Mass and energy resolved detection of ions and neutral sputtered species incident at the substrate during reactive magnetron sputtering of Ti in mixed $Ar+N_2$ mixtures, Journal of Vacuum Science & Technology A 12 (5) (1994) 2846–2854.
[16] G. Håkansson, J.E. Sundgren, D. McIntyre, J.E. Greene, W.D. Münz, Microstructure and physical properties of polycrystalline metastable $Ti_{0.5}Al_{0.5}N$ alloys grown by d.c. magnetron sputter deposition, Thin Solid Films 153 (1) (1987) 55–65.
[17] I. Petrov, P.B. Barna, L. Hultman, J.E. Greene, Microstructural evolution during film growth, Journal of Vacuum Science & Technology A 21 (5) (2003) S117–S128.
[18] L. Hultman, J.E. Sundgren, J.E. Greene, D.B. Bergstrom, I. Petrov, High-flux low-energy (≈20 eV) N^{+2} ion irradiation during TiN deposition by reactive magnetron sputtering: Effects on microstructure and preferred orientation, Journal of Applied Physics 78 (9) (1995) 5395–5403.

[19] F. Adibi, I. Petrov, J.E. Greene, L. Hultman, J.E. Sundgren, Effects of high-flux low-energy (20–100 eV) ion irradiation during deposition on the microstructure and preferred orientation of $Ti_{0.5}Al_{0.5}N$ alloys grown by ultra-high-vacuum reactive magnetron sputtering, Journal of Applied Physics 73 (12) (1993) 8580–8589.

[20] H. Windischmann, Intrinsic stress in sputter-deposited thin films, Critical Reviews in Solid State and Materials Sciences 17 (6) (1992) 547–596.

[21] I. Petrov, L. Hultman, U. Helmersson, J.E. Sundgren, J.E. Greene, Microstructure modification of TiN by ion bombardment during reactive sputter deposition, Thin Solid Films 169 (2) (1989) 299–314.

[22] H. Ljungcrantz, L. Hultman, J.E. Sundgren, S. Johansson, N. Kristensen, J.Å. Schweitz, C.J. Shute, Residual stresses and fracture properties of magnetron sputtered Ti films on Si microelements, Journal of Vacuum Science & Technology A 11 (3) (1993) 543–553.

[23] G. Greczynski, S. Mráz, J.M. Schneider, L. Hultman, Metal-ion subplantation: A game changer for controlling nanostructure and phase formation during film growth by physical vapor deposition, Journal of Applied Physics 127 (18) (2020) 180901.

[24] G. Greczynski, S. Mráz, H. Ruess, M. Hans, J. Lu, L. Hultman, J.M. Schneider, Extended metastable Al solubility in cubic VAlN by metal-ion bombardment during pulsed magnetron sputtering: film stress vs subplantation, Journal of Applied Physics 122 (2) (2017) 025304.

[25] G. Greczynski, S. Mráz, L. Hultman, J.M. Schneider, Selectable phase formation in VAlN thin films by controlling Al^+ subplantation depth, Scientific Reports 7 (1) (2017) 17544.

[26] H. Rueß, D. Music, A. Bahr, J.M. Schneider, Effect of chemical composition, defect structure, and stress state on the elastic properties of $(V_{1-x}Al_x)_{1-y}N_y$, Journal of Physics: Condensed Matter 32 (2) (2019) 025901.

[27] D. Music, L. Banko, H. Ruess, M. Engels, A. Hecimovic, D. Grochla, D. Rogalla, T. Brögelmann, A. Ludwig, A.v. Keudell, K. Bobzin, J.M. Schneider, Correlative plasma-surface model for metastable Cr-Al-N: Frenkel pair formation and influence of the stress state on the elastic properties, Journal of Applied Physics 121 (21) (2017) 215108.

[28] M. Hans, L. Patterer, D. Music, D.M. Holzapfel, S. Evertz, V. Schnabel, B. Stelzer, D. Primetzhofer, B. Völker, B. Widrig, A.O. Eriksson, J. Ramm, M. Arndt, H. Rudigier, J.M. Schneider, Stress-Dependent Elasticity of TiAlN Coatings, Coatings 9 (1) (2019) 24.

[29] P. Sigmund, Sputtering by ion bombardment theoretical concepts, in: R. Behrisch (Ed.), Sputtering by Particle Bombardment I: Physical Sputtering of Single-Element Solids, Springer Berlin Heidelberg, Berlin, Heidelberg, 1981, pp. 9–71.

[30] H. Oettel, R. Wiedemann, Residual stresses in PVD hard coatings, Surface and Coatings Technology 76-77 (1995) 265–273.

[31] F.M. D'Heurle, J.M.E. Harper, Note on the origin of intrinsic stresses in films deposited via evaporation and sputtering, Thin Solid Films 171 (1) (1989) 81–92.

[32] L. Hultman, Thermal stability of nitride thin films, Vacuum 57 (1) (2000) 1–30.

[33] B. Alling, A. Karimi, L. Hultman, I.A. Abrikosov, First-principles study of the effect of nitrogen vacancies on the decomposition pattern in cubic $Ti_{1-x}A_{lx}N_{1-y}$, Applied Physics Letters 92 (7) (2008) 071903.

[34] K. Grönhagen, J. Ågren, M. Odén, Phase-field modelling of spinodal decomposition in TiAlN including the effect of metal vacancies, Scripta Materialia 95 (2015) 42–45.

[35] M. to Baben, L. Raumann, D. Music, J.M. Schneider, Origin of the nitrogen over- and understoichiometry in $Ti_{0.5}Al_{0.5}N$ thin films, Journal of Physics: Condensed Matter 24 (15) (2012) 155401.

[36] A.B. Mei, H. Kindlund, E. Broitman, L. Hultman, I. Petrov, J.E. Greene, D.G. Sangiovanni, Adaptive hard and tough mechanical response in single-crystal B1 VN_x ceramics via control of anion vacancies, Acta Materialia 192 (2020) 78–88.

[37] A.J. Perry, On the existence of point defects in physical vapor deposited films of TiN, ZrN, and HfN, Journal of Vacuum Science & Technology A 6 (3) (1988) 2140–2148.

[38] D. Music, L. Offermann, G. Aras, P. Bliem, M. Geilen, Y. Naunheim, T. Ravindra, Theoretical study of deposition-induced point defects in ZnO, Surface and Coatings Technology 309 (2017) 531–535.

[39] D. Music, F. Nahif, K. Sarakinos, N. Friederichsen, J.M. Schneider, Ab initio molecular dynamics of Al irradiation-induced processes during Al_2O_3 growth, Applied Physics Letters 98 (11) (2011) 111908.

[40] H.Y. Xiao, Y. Zhang, W.J. Weber, *Ab initio* molecular dynamics simulations of low-energy recoil events in ThO_2, CeO_2, and ZrO_2, Physical Review B 86 (5) (2012) 054109.

[41] Y. Zhang, H.J. Whitlow, T. Winzell, I.F. Bubb, T. Sajavaara, K. Arstila, J. Keinonen, Detection efficiency of time-of-flight energy elastic recoil detection analysis systems, Nuclear Instruments and Methods in Physics Research Section B: Beam Interactions with Materials and Atoms 149 (4) (1999) 477–489.

[42] M. Hans, H. Rueß, Z. Czigány, J. Krause, P. Ondračka, D. Music, S. Evertz, D.M. Holzapfel, D. Primetzhofer, J.M. Schneider, Spinodal decomposition of reactively sputtered $(V_{0.64}Al_{0.36})_{0.49}N_{0.51}$ thin films, Surface and Coatings Technology 389 (2020) 125641.

[43] M. Janson, CONTES Conversion of Time-energy Spectra a Program for ERDA Data Analysis (Internal Report, Uppsala University), Uppsala, 2004.

[44] M. Yasaka, X-ray thin-film measurement techniques, The Rigaku Journal 26 (2) (2010) 1–9.

[45] B.D. Cullity, Elements of X-ray Diffraction, Addison-Wesley Publishing1956.

[46] R.R. Reeber, K. Wang, Thermal expansion and lattice parameters of group IV semiconductors, Materials Chemistry and Physics 46 (2) (1996) 259–264.

[47] W.C. Oliver, G.M. Pharr, An improved technique for determining hardness and elastic modulus using load and displacement sensing indentation experiments, Journal of Materials Research 7 (6) (2011) 1564–1583.

[48] P. Hohenberg, W. Kohn, Inhomogeneous Electron Gas, Physical Review 136 (3B) (1964) B864–B871.

[49] T. Ozaki, H. Kino, Efficient projector expansion for the ab initio LCAO method, Physical Review B 72 (4) (2005) 045121.

[50] T. Ozaki, Variationally optimized atomic orbitals for large-scale electronic structures, Physical Review B 67 (15) (2003) 155108.

[51] J.P. Perdew, K. Burke, M. Ernzerhof, Generalized Gradient Approximation Made Simple, Physical Review Letters 77 (18) (1996) 3865–3868.

[52] T. Ozaki, H. Kino, Numerical atomic basis orbitals from H to Kr, Physical Review B 69 (19) (2004) 195113.

[53] G.H. Kinchin, R.S. Pease, The Displacement of Atoms in Solids by Radiation, Reports on Progress in Physics 18 (1) (1955) 1–51.

[54] D.G. Sangiovanni, B. Alling, P. Steneteg, L. Hultman, I.A. Abrikosov, Nitrogen vacancy, self-interstitial diffusion, and Frenkel-pair formation/dissociation in *B1* TiN studied by *ab initio* and classical molecular dynamics with optimized potentials, Physical Review B 91 (5) (2015) 054301.

[55] K. Momma, F. Izumi, VESTA: a three-dimensional visualization system for electronic and structural analysis, Journal of Applied Crystallography 41 (3) (2008) 653–658.

[56] F. Birch, Finite strain isotherm and velocities for single-crystal and polycrystalline NaCl at high pressures and 300°K, Journal of Geophysical Research: Solid Earth 83 (B3) (1978) 1257–1268.

[57] P. Söderlind, L. Nordström, Y. Lou, B. Johansson, Relativistic effects on the thermal expansion of the actinide elements, Physical Review B 42 (7) (1990) 4544–4552.

[58] R. Hill, The Elastic Behaviour of a Crystalline Aggregate, Proceedings of the Physical Society. Section A 65 (5) (1952) 349–354.

[59] D. Holec, L. Zhou, H. Riedl, C.M. Koller, P.H. Mayrhofer, M. Friák, M. Šob, F. Körmann, J. Neugebauer, D. Music, M.A. Hartmann, F.D. Fischer, Atomistic Modeling-Based Design of Novel Materials Advanced Engineering Materials 19(4) (2017) 1600688.

[60] G. Greczynski, I. Petrov, J.E. Greene, L. Hultman, Strategy for tuning the average charge state of metal ions incident at the growing film during HIPIMS deposition, Vacuum 116 (2015) 36–41.

[61] S. Mráz, J.M. Schneider, Influence of the negative oxygen ions on the structure evolution of transition metal oxide thin films, Journal of Applied Physics 100 (2) (2006) 023503.

[62] Y. Jiang, S. Mráz, J.M. Schneider, Growth of V–Al–C thin films by direct current and high power impulse magnetron sputtering from a powder metallurgical composite target, Thin Solid Films 538 (2013) 1–6.

[63] M. Aiempanakit, A. Aijaz, D. Lundin, U. Helmersson, T. Kubart, Understanding the discharge current behavior in reactive high power impulse magnetron sputtering of oxides, Journal of Applied Physics 113 (13) (2013) 133302.

[64] F. Rovere, D. Music, S. Ershov, M. to Baben, H.-G. Fuss, P.H. Mayrhofer, J.M. Schneider, Experimental and computational study on the phase stability of Al-containing cubic transition metal nitrides, Journal of Physics D: Applied Physics 43 (3) (2010) 035302.

[65] A. Forslund, A. Ruban, Surface energetics of $Al_xTi_{1-x}N$ alloys, Computational Materials Science 183 (2020) 109813.

[66] J.E. Greene, J.E. Sundgren, L. Hultman, I. Petrov, D.B. Bergstrom, Development of preferred orientation in polycrystalline TiN layers grown by ultrahigh vacuum reactive magnetron sputtering, Applied Physics Letters 67 (20) (1995) 2928–2930.

[67] J.S. Chun, I. Petrov, J.E. Greene, Dense fully 111-textured TiN diffusion barriers: Enhanced lifetime through microstructure control during layer growth, Journal of Applied Physics 86 (7) (1999) 3633–3641.

[68] D. Gall, I. Petrov, N. Hellgren, L. Hultman, J.E. Sundgren, J.E. Greene, Growth of poly- and single-crystal ScN on MgO(001): Role of low-energy N^{+2} irradiation in determining texture, microstructure evolution, and mechanical properties, Journal of Applied Physics 84 (11) (1998) 6034–6041.

[69] J.-H. Huang, C.-H. Lin, G.-P. Yu, Texture evolution of vanadium nitride thin films, Thin Solid Films 688 (2019) 137415.

[70] A. Anders, A structure zone diagram including plasma-based deposition and ion etching, Thin Solid Films 518 (15) (2010) 4087–4090.

[71] C.V. Falub, A. Karimi, M. Ante, W. Kalss, Interdependence between stress and texture in arc evaporated Ti–Al–N thin films, Surface and Coatings Technology 201 (12) (2007) 5891–5898.

[72] P.H. Mayrhofer, G. Tischler, C. Mitterer, Microstructure and mechanical/thermal properties of Cr–N coatings deposited by reactive unbalanced magnetron sputtering, Surface and Coatings Technology 142-144 (2001) 78–84.

[73] L. Tsetseris, N. Kalfagiannis, S. Logothetidis, S.T. Pantelides, Structure and interaction of point defects in transition-metal nitrides, Physical Review B 76 (22) (2007) 224107.

[74] C.A. Davis, A simple model for the formation of compressive stress in thin films by ion bombardment, Thin Solid Films 226 (1) (1993) 30–34.

[75] D.R. McKenzie, Generation and applications of compressive stress induced by low energy ion beam bombardment, Journal of Vacuum Science & Technology B: Microelectronics and Nanometer Structures Processing, Measurement, and Phenomena 11 (5) (1993) 1928–1935.

[76] G.V. Sin'ko, N.A. Smirnov, On elasticity under pressure, Journal of Physics: Condensed Matter 16 (45) (2004) 8101–8104.

[77] F. Herrig, D. Music, H. Rueß, A.L. Ravensburg, P.J. Pöllmann, J.M. Schneider, Chemical composition and stress dependence of the elastic properties of κ-$(Fe,Mn)_3AlC$ thin films, Scripta Materialia 153 (2018) 49–53.